


RESEARCH ARTICLE

[View Article Online](#)
[View Journal](#) | [View Issue](#)

 Cite this: *Inorg. Chem. Front.*, 2023, **10**, 2799

Dual-ligand-functionalized dodeca-nuclear lanthanide–tungsten-cluster incorporated selenotungstates and fluorescence detection of dipicolinic acid (an anthrax biomarker)†

 Tiantian Gong, Sen Yang, Zixu Wang, Mengyao Li, Siyu Zhang, Jiancai Liu,*
 Lijuan Chen* and Junwei Zhao *

A series of rigid–flexible-ligand functionalized dodeca-nuclear lanthanide–tungsten heterometal cluster incorporated ring-shaped selenotungstates $[\text{H}_2\text{N}(\text{CH}_3)_2]_{16}\text{Na}_2[\text{Ln}_4(\text{H}_2\text{O})_6(\text{HPZDA})_2(\text{HFMA})_2\text{W}_8\text{O}_{21}][\text{B}-\alpha\text{-SeW}_9\text{O}_{33}]_4\cdot 29\text{H}_2\text{O}$ [$\text{Ln} = \text{Ce}^{3+}$ (**1**), Pr^{3+} (**2**), Nd^{3+} (**3**); $\text{H}_2\text{PZDA} = 2,3$ -pyrazine dicarboxylic acid, $\text{H}_2\text{FMA} = \text{fumaric acid}$] and $[\text{H}_2\text{N}(\text{CH}_3)_2]_{14}\text{Cs}_2\text{Na}_2[\text{Eu}_4(\text{H}_2\text{O})_6(\text{HPZDA})_2(\text{HFMA})_2\text{W}_8\text{O}_{21}][\text{B}-\alpha\text{-SeW}_9\text{O}_{33}]_4\cdot 30\text{H}_2\text{O}$ (**4**) were prepared by a cooperative strategy of rigid and flexible ligands. The polyanion skeletons of **1–4** comprise an inorganic–organic hybrid dodeca-nuclear $[\text{Ln}_4(\text{H}_2\text{O})_6(\text{HPZDA})_2(\text{HFMA})_2\text{W}_8\text{O}_{21}]^{14+}$ heterometallic cluster surrounded by four trivalent Keggin $[\text{B}-\alpha\text{-SeW}_9\text{O}_{33}]^{8-}$ subunits in a rectangle-like arrangement. Based on its fluorescence properties, **4** was used as a fluorescent probe for detecting an anthrax biomarker dipicolinic acid (DPA) with a low limit of detection, and excellent selectivity and anti-interference. The possible fluorescence enhancement mechanism of **4** in the process of detecting DPA may stem from energy transfer from DPA to Eu^{3+} ions in **4**, which can be confirmed by decay lifetime measurements of **4** in H_2O and D_2O with and without DPA, and a positive signal of the partial substitution of H_2O ligands on Eu^{3+} ions by DPA ligands. This work proposes a feasible cooperative strategy of rigid and flexible ligands for constructing new structural types of polyoxometalate hybrids, and also provides some meaningful insights into efficient biomolecule detection by utilizing polyoxometalate-based luminescence materials.

 Received 24th February 2023,
 Accepted 1st April 2023

DOI: 10.1039/d3qi00361b

rsc.li/frontiers-inorganic

Introduction

The design and fabrication of inorganic–organic hybrid fluorescence materials have drawn considerable attention in view of their wide applications in optical devices, displays, cell imaging, sensing, laser lighting, and so on.^{1,2} Such materials combining inorganic and organic components can overcome the drawbacks of a single component and have a synergistic effect between two components. For example, the sensitization of lanthanide emissions by organic chromophores can play an important role in developing function-oriented structural assembly, functional complementation and performance optimization.^{3–5}

Polyoxometalates (POMs) are a class of inorganic metal–oxo clusters and have exhibited their rich architectural diversity

and fascinating properties in optics, catalysis, magnetism, biomedicine, nanotechnology, *etc.*^{6–11} As the most widely researched branch of POMs, polyoxotungstates (POTs), particularly inorganic–organic hybrid POT materials (IOHPMs), have attracted ongoing research interest.^{12,13} In this respect, the persistent pursuit of IOHPMs was driven by the strong combining capacity of organic ligands towards metal centers or POTs, where organic ligands can provide abundant binding sites and modes for their coordination assembly by subtly acclimating themselves to the whole geometrical requirements.^{14–17} Flexible organic ligands feature alkyl carbon-chain backbones with carboxyl, hydroxyl or amino groups and can bend or rotate freely around single bonds, whereas rigid organic ligands usually possess an aromatic or heterocyclic backbone that makes them spatially limited and oriented.^{18–20} Notably, flexible or rigid ligands serving as chelating or bridging linkers have been extensively applied to a POT system and have demonstrated their outstanding potential for the fabrication of high-nuclear metal-substituted or extended IOHPMs.^{5,21,22} However, mixed-ligand-participated IOHPMs remain underexplored. For instance, the great potential of organic ligands applied to the POT system has been shown in the design and

Henan Key Laboratory of Polyoxometalate Chemistry, College of Chemistry and Chemical Engineering, Henan University, Kaifeng 475004, China.

E-mail: liujiancai@henu.edu.cn, ljchen@henu.edu.cn, zhaojunwei@henu.edu.cn

† Electronic supplementary information (ESI) available. CCDC 2244122–2244125 (1–4). For ESI and crystallographic data in CIF or other electronic format see

DOI: <https://doi.org/10.1039/d3qi00361b>

assembly of POT–organic frameworks based on inorganic–organic Ni₆-substituted {Ni₆(μ₃-OH)₃(H₂O)₆Ln(B-α-PW₉O₃₄)} building blocks (BBs) (Fig. 1a and b).²³

According to the soft–hard acid–base rule, ligands with N/O donors have close affinity with hard lanthanide (Ln) cations. Thus, the introduction of Ln ions can provide more opportunities for assembling structures and discovering properties.^{24–29} As can be seen in a dual-ligand-functionalized Ln-incorporated POT {[Cu(en)₂][Cu(en)₂(H₂O)][(α-H₂SiW₁₁O₃₉)Dy(H₂O)(PZDA)]₂}^{6–} (en = ethylenediamine) (Fig. 1c and d), each tetradentate PZDA^{2–} ligand coordinates to two Dy³⁺ ions and one [Cu(en)₂]²⁺ ion by one N and three carboxyl O atoms.³⁰ In 2017, Zhao *et al.* reported a series of novel Ln–organometal co-encapsulated tellurotungstates {[Sn(CH₃W₂O₄(IN))[(B-α-TeW₈O₃₁)Ln(H₂O)(CH₃COO)]₂}^{20–} (Ln = Ce³⁺–Tb³⁺; CH₃COOH = acetic acid, HIN = isonicotinic acid), in which the IN[–] ligand is combined with one {W₂O₄} fragment and one CH₃COO[–]-decorated Ln³⁺ ion (Fig. 1e and f).³¹ In 2019, Song *et al.* reported rarely seen four-ligand-participating Fe–Ln-heterometallic tellurotungstates [Ln₂(CH₃COO)₂(H₂O)₄Fe₂(HPDCA)₂(B-β-TeW₉O₃₃)₂][Ln₂(H₂O)₈Fe₂(HPDCA)₂(B-β-TeW₉O₃₃)₂]^{14–} (Ln = Eu³⁺, Tb³⁺, Dy³⁺, Er³⁺; H₂PDCA = 2,5-pyridine-dicarboxylic acid). Fig. 1g and h display a one-dimensional chain arrangement assembled from tetrameric structural units bridged by HPDCA[–] linkers.³² Overall, reports on metal-functionalized IOHPMs (MFIOHPMs) with mixed flexible and rigid ligands are relatively less. Therefore, preparing new-type high-nuclear or extended MFIOHPMs modulated by flexible–rigid co-ligands and exploring their properties are of great

significance for the sustainable development of POM chemistry.

Based on the above considerations, we are very interested in the synthetic probability by utilizing *in situ* formed vacant POT units to react with Ln ions in the presence of rigid and flexible ligands to construct novel mixed-organic ligand functionalized MFIOHPMs with innovative structures and fascinating properties. Firstly, the stereo-directed [SeO₃]^{2–} heteroanion with a lone pair of electrons in the presence of tungstates is used to stimulate the generation of negatively charged lacunary selenotungstate (ST) units, which can grasp more positive Ln ions for polymeric assembly. Secondly, flexible fumaric acid (H₂FMA) with two carboxyl groups, and rigid 2,3-pyrazine dicarboxylic acid (H₂PZDA) with two carboxyl groups and two pyrazine-N atoms possess rich coordination modes and strong coordination preference to Ln and W centers, and are also conducive to building up hybrid aggregates. In addition, *in situ* formed POT units and introduced organic ligands are generally used as inorganic and organic chromophores to sensitize the emission of Ln ions, which can provide the optical application potentiality of the desired mixed-organic ligand functionalized MFIOHPMs.^{5,31} As expected, a series of unique dual-ligand functionalized dodeca-nuclear Ln–W-cluster incorporated [H₂N(CH₃)₂]₁₆Na₂[Ln₄(H₂O)₆(HPZDA)₂(HFMA)₂W₈O₂₁][B-α-SeW₉O₃₃]₄·29H₂O [Ln = Ce³⁺ (1), Pr³⁺ (2), Nd³⁺ (3)] and [H₂N(CH₃)₂]₁₄Cs₂Na₂[Eu₄(H₂O)₆(HPZDA)₂(HFMA)₂W₈O₂₁][B-α-SeW₉O₃₃]₄·30H₂O (4) are successfully prepared, whose polyanions are constructed from four trivacant Keggin [B-α-SeW₉O₃₃]^{8–} subunits encapsulating an inorganic–organic

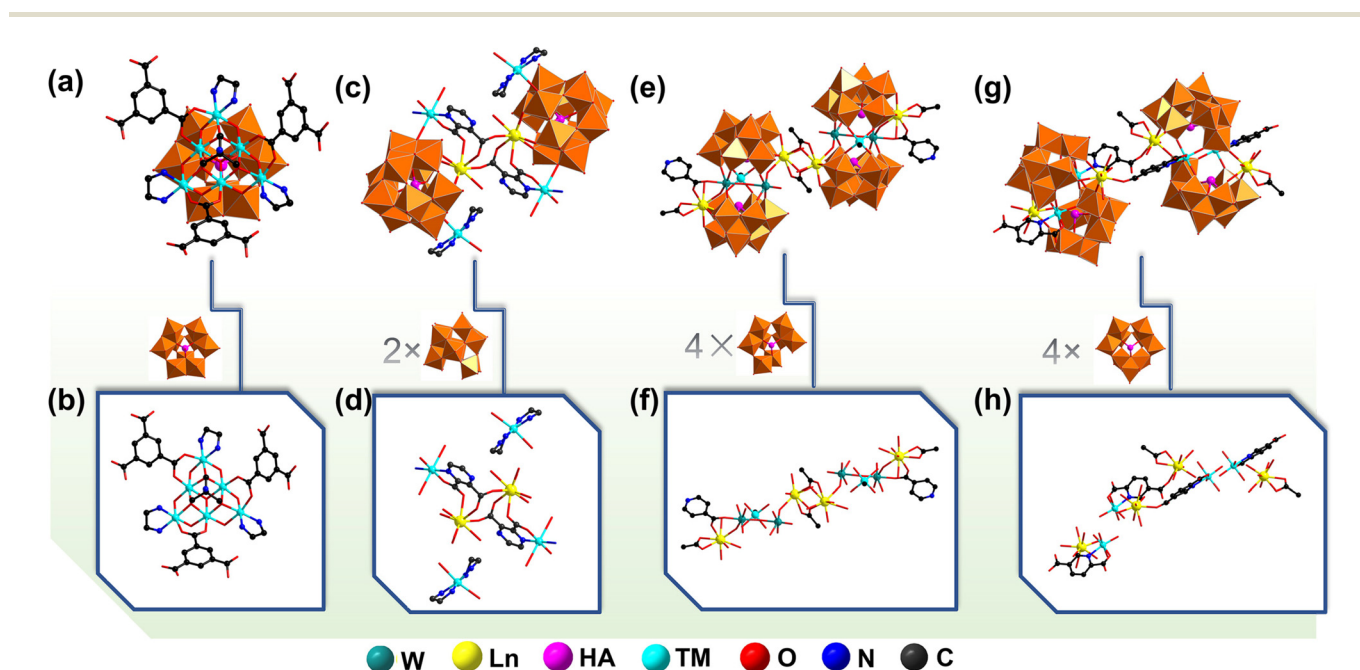


Fig. 1 Summary of representative structures of IOHPMs. (a and b) View of {Ni₆(Tris)(en)₃(BTC)₃(B-α-PW₉O₃₄)} (Tris = tris(hydroxymethyl)amino-methane, en = ethylenediamine) and its remaining part without {B-α-PW₉O₃₄}. (c and d) View of {[Cu(en)₂]₂[Cu(PZDA)₂][(α-H₂SiW₁₁O₃₉)Ce(H₂O)]₂}^{6–} and its remaining part without {α-H₂SiW₁₁O₃₉}. (e and f) View of {[Sn(CH₃)W₂O₄(IN)][(B-α-TeW₈O₃₁)Ln(H₂O)(CH₃COO)]₂}^{20–} and its remaining part without {B-α-TeW₈O₃₁}. (g and h) View of [Ln₂(CH₃COO)₂(H₂O)₄Fe₂(HPDCA)₂(B-β-TeW₉O₃₃)₂][Ln₂(H₂O)₈Fe₂(HPDCA)₂(B-β-TeW₉O₃₃)₂]^{14–} and its remaining part without {B-β-TeW₉O₃₃}.

hybrid dodeca-nuclear $[\text{Ln}_4(\text{H}_2\text{O})_6(\text{HPZDA})_2(\text{HFMA})_2\text{W}_8\text{O}_{21}]^{14+}$ heterometal cluster. Intriguingly, the coexistence of rigid HPZDA^- and flexible HFMA^- ligands allows diverse coordination of pyrazine-N and carboxy-O sites to both or either of Ln and W centers, leading to the versatile generation of dual-ligand-functionalized high-nuclear heterometallic clusters, accompanied by the formation of five-, six- and seven-membered rings in the structures. Interestingly, **4** emits remarkable fluorescence (FL) and can be applied as a FL probe to detect a typical anthrax biomarker dipicolinic acid (DPA); it exhibits a low detection limit (3.83 μM), a rapid respond time (10 s) and outstanding selectivity and anti-interference. When it is applied in a practical complex environment, the **4**-based FL sensor still exhibits good detection activity and acceptable recovery ranges. Moreover, the possible mechanism of recognizing DPA is studied. This research shows the good application potentiality of rigid and flexible-ligand functionalized MFIOHPMs in the aspect of FL detection of the anthrax biomarker DPA.

Results and discussion

Synthesis

Through relevant investigations on STs, it is found that the one-pot self-assembly reaction is a suitable and effective synthetic strategy for preparing novel ST derivatives.^{33,34} Also, besides the delicate regulation on reaction parameters such as the molar ratio of reactants and reaction temperature, the acidic pH window from 3 to 5 is more favorable for the generation of “open” lacunary ST units.^{35,36} On the basis of a previous work, **1–4** were obtained by the reaction of $\text{Na}_2\text{WO}_4 \cdot 2\text{H}_2\text{O}$, Na_2SeO_3 , $\text{Ln}(\text{NO}_3)_3 \cdot 6\text{H}_2\text{O}$ ($\text{Ln} = \text{Ce}^{3+}$, Pr^{3+} , Nd^{3+} , Eu^{3+}), H_2PZDA , H_2FMA , CH_3COOH and dimethylamine hydrochloride in aqueous solution ($\text{pH} = 3$). For **4**, CsCl was added to the reaction system for growing good-quality crystals. However, parallel experiments revealed that the introduction of CH_3COOH guarantees a relatively clear reaction system and the formation of high-quality crystals with high yield. Otherwise, a large amount of amorphous precipitate was formed during the crystal growth process, so the crystal yield was greatly reduced. We speculated that CH_3COOH could not only work as an acid regulator, but also work as an organic solubilizer to ameliorate the reactivity of Ln and tungstates.³⁷ Thus, CH_3COOH is an indispensable starting material in the synthesis of **1–4**. Besides, much attention was also paid to other reaction factors including pH, the ratio of W : Se and the usage of $\text{Ln}(\text{NO}_3)_3 \cdot 6\text{H}_2\text{O}$. Comparative experiments showed that the pH range of 2.8–3.5 is conducive to crystal generation; in particular, a pH value of 3 is the optimal value. The ratio of W : Se between 17.5 and 32.8 favors the generation of **1–4**, and the optimum ratio is 25.97. In addition, the dosage of $\text{Ln}(\text{NO}_3)_3 \cdot 6\text{H}_2\text{O}$ between 0.450 and 0.700 g results in the successful formation of **1–4** and the highest yield was achieved when the amount was around 0.500 g. Moreover, the addition of CsCl greatly promoted the good crystallinity of **4**.

Structural description

The experimental XRD patterns coincide well with their corresponding simulated patterns, illustrating the good phase purity of **1–4** (Fig. S1†). The IR and TG tests of **1–4** have been recorded for structural characterization (Fig. S2 and S3†).

The crystallographic structural parameters of **1–4** are summarized in Table S1.† As the structures of **1–4** are similar, only the structure of **4** will be discussed in detail here. **4** consists of an unusual rigid-flexible-ligand functionalized multi-metal-stabilized tetrameric polyanion $[\text{Eu}_4(\text{H}_2\text{O})_6(\text{HPZDA})_2(\text{HFMA})_2\text{W}_8\text{O}_{21}][\text{B-}\alpha\text{-SeW}_9\text{O}_{33}]_4^{18-}$ (**4a**, Fig. 2a). In the tetrameric **4a** polyanion, four trivalent Keggin subunits $[\text{B-}\alpha\text{-SeW}_9\text{O}_{33}]^{8-}$ ($\{\text{SeW}_9\}$) are aligned in a rectangle-like mode and connected by a dodeca-nuclear heterometal cluster $[\text{Eu}_4(\text{H}_2\text{O})_6(\text{HPZDA})_2(\text{HFMA})_2\text{W}_8\text{O}_{21}]^{14+}$ ($\{\text{Eu}_4(\text{HPZDA})_2(\text{HFMA})_2\text{W}_8\}$) through W–O–W and W–O–Eu linkers into a novel ring-shaped architecture. The heterometal cluster is situated at the center of **4a** (Fig. 2b), whilst the O2 atom is the center of symmetry of the whole polyanion (Fig. S4†). Remarkably, the exposed vacancies of each trivalent $\{\text{SeW}_9\}$ subunit are filled with W and Eu centers. For better understanding the assembly of peripheral $\{\text{SeW}_9\}$ subunits (labelled as I, II, IA and IIA) and the internal $\{\text{Eu}_4(\text{HPZDA})_2(\text{HFMA})_2\text{W}_8\}$ cluster, the tetrameric **4a** polyanion can be simplified and displayed in two more perspicuous ways by breaking up the intricate $\{\text{Eu}_4(\text{HPZDA})_2(\text{HFMA})_2\text{W}_8\}$ core (Fig. 2c–e). One way is the connection of I, II, IA and IIA $\{\text{SeW}_9\}$ subunits by the HFMA^- -decorated hourglass-like hexa-W cluster $[\text{W}_6\text{O}_{17}(\text{HFMA})_2]$ ($\{\text{W}_6(\text{HFMA})_2\}$), where the adjacent I and II $\{\text{SeW}_9\}$ subunits are grasped together by W2 and W8 ions into a dimer, and two dimers are further concatenated with each other through O–W11–O bonds to generate the tetramer (Fig. 2d). The other way is the fusion of I, II, IA and IIA $\{\text{SeW}_9\}$ subunits by the HPZDA -bridged annular hexa-nuclear heterometal cluster $[\text{Eu}_4(\text{H}_2\text{O})_6(\text{HPZDA})_2\text{W}_2\text{O}_4]^{14+}$ ($\{\text{Eu}_4(\text{HPZDA})_2\text{W}_2\}$), where Eu^{3+} and Eu^{2+} ions are respectively encapsulated into the pockets of II and I $\{\text{SeW}_9\}$ subunits into a C-shaped dimer and two dimers directly coordinate with rigid HPZDA^- ligands with the support of pyrazine N and carboxylic O sites into a tetramer (Fig. 2e). Thus, the double bridging roles of the hexa-nuclear $\{\text{W}_6(\text{HFMA})_2\}$ cluster and hexa-nuclear $\{\text{Eu}_4(\text{HPZDA})_2\text{W}_2\}$ ring lead to the aggregation of four $\{\text{SeW}_9\}$ subunits, ultimately forming the neoteric and stable assembly of the **4a** polyanion.

One prominent characteristic of **4a** is the existence of the interesting dodeca-nuclear heterometallic $\{\text{Eu}_4(\text{HPZDA})_2(\text{HFMA})_2\text{W}_8\}$ cluster, comprising four Eu^{III} ions, eight W^{VI} centers, two HPZDA^- ligands and two HFMA^- ligands (Fig. 2f). The dodeca-nuclear cluster can be reckoned as the combination of a $\{\text{W}_6(\text{HFMA})_2\}$ unit and a $\{\text{Eu}_4(\text{HPZDA})_2\text{W}_2\}$ ring by four pairs of Eu–O–W bonds, where the $\{\text{W}_6(\text{HFMA})_2\}$ cluster is interpenetrated with the ring (Fig. 2g). Interestingly, the $\{\text{W}_6(\text{HFMA})_2\}$ cluster links to a “hourglass” by superimposing W11 and W11A atoms together, where the top and the bottom are two identical mono- HFMA^- -chelating $\{\text{W}_3\text{O}_8(\text{HFMA})\}$ units interconnected by sharing the O2 atom (Fig. S5†). For the

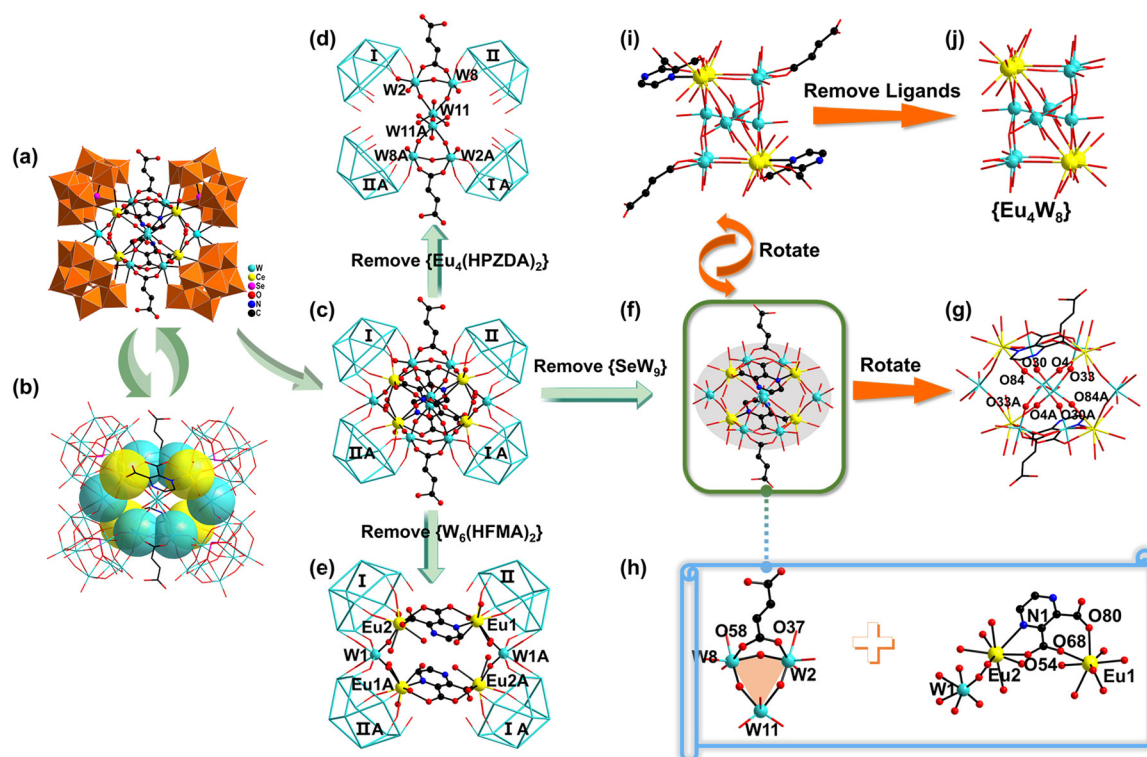


Fig. 2 (a) Tetrameric **4a** polyanion. (b) Highlighted $\{\text{Eu}_4(\text{HPZDA})_2(\text{HFMA})_2\text{W}_8\}$ cluster in **4a**. (c) Simplified structure of **4a**. (d) Connection mode of four $\{\text{SeW}_9\}$ subunits and the central $\{\text{W}_6(\text{HFMA})_2\}$ cluster. (e) Connection mode of four $\{\text{Eu}_2(\text{HPZDA})\}$ subunits and the central $\{\text{Eu}_4(\text{HPZDA})_2\text{W}_2\}$ cluster. (f) Top view of the $\{\text{Eu}_4(\text{HPZDA})_2(\text{HFMA})_2\text{W}_8\}$ cluster. (g) Highlighted O bridges in the $\{\text{Eu}_4(\text{HPZDA})_2(\text{HFMA})_2\text{W}_8\}$ cluster. (h) View of $\{\text{W}_3\text{O}_8(\text{HFMA})\}$ and $\{\text{Eu}_2(\text{HPZDA})\}$ subunits. (i) Side view of the $\{\text{Eu}_4(\text{HPZDA})_2(\text{HFMA})_2\text{W}_8\}$ cluster. (j) The remaining part of the $\{\text{Eu}_4(\text{HPZDA})_2(\text{HFMA})_2\text{W}_8\}$ cluster by removing organic ligands.

$\{\text{W}_3\text{O}_8(\text{HFMA})\}$ unit, both O58 and O37 atoms in one carboxyl group of the flexible HFMA^- ligand participate in the coordination of W8 and W2 atoms, producing an uncommon “-C-O-W-O-W-O-” six-membered ring, almost perpendicular to the apex-O-linked- W_3 -based triangle (Fig. 2h). The $\{\text{Eu}_4(\text{HPZDA})_2\text{W}_2\}$ ring is composed of two mono-HPZDA⁻-chelating $\{\text{Eu}_2(\text{HPZDA})\}$ units alternately linked by two W atoms (W1 and W1A). In each $\{\text{Eu}_2(\text{HPZDA})\}$ unit, the multidentate HPZDA⁻ ligand simultaneously chelates with $\text{Eu}1^{3+}$ and $\text{Eu}2\text{A}^{3+}$ ions *via* N and O coordination sites, where the $\text{Eu}1^{3+}$ ion is bonded to two O atoms (O68 and O80) from two carboxyl groups to form an unusual “-C-C-O-Eu-O-C-C-” seven-membered ring, whilst the $\text{Eu}2^{3+}$ ion is firmly grasped by one N (N1) and one neighboring carboxyl O atom (O54) to form a classical “-N-C-C-O-Eu-” five-membered ring (Fig. S6[†]). Thus, it can be seen that the employment of rigid and flexible organic ligands with abundant N- and O binding sites offers more possibilities for synthesizing organically functionalized Ln-incorporated POM hybrids and discovering more interesting and versatile coordination assembly modes.³⁸ Moreover, two crystallographically unique Eu^{3+} ions in **4a** have two different geometries. Specifically, the $\text{Eu}1^{3+}$ ion has an octa-coordinate bi-capped triangular prism geometry that is formed by two O atoms (O28, O34) from one $\{\text{SeW}_9\}$ subunit, three O atoms (O4, O22 and O33) from three central $\{\text{WO}_6\}$ octahedra,

one water molecule (O1W), and two carboxyl O atoms (O68, O80) of the HPZDA⁻ ligand [$\text{Eu}1\text{-O}$: 2.327(11)–2.498(14) Å] (Fig. S7a[†]). Distinctly, the $\text{Eu}2^{3+}$ ion is surrounded by two O atoms (O19, O52) belonging to one $\{\text{SeW}_9\}$ subunit, three O atoms (O26, O30 and O84) from the central $\{\text{WO}_6\}$ octahedra, two water molecules (O2W, O3W), and one N atom and one carboxyl O atom from the HPZDA⁻ ligand, adopting a nine-coordinate tri-capped triangular prism geometry [$\text{Eu}2\text{-O}$: 2.379(13)–2.543(14) Å, $\text{Eu}2\text{-N}$: 2.685(17) Å] (Fig. S7b[†]).

A further rotation of the dodeca-nuclear $\{\text{Eu}_4(\text{HPZDA})_2(\text{HFMA})_2\text{W}_8\}$ cluster produces a visual “cuboid”, but an irregular polyhedron (Fig. 2i and S8[†]), offering a new perspective on this structure. By removing all ligands that hang on the top and the bottom of the visual “cuboid”, a $\{\text{Eu}_4\text{W}_8\}$ unit consisting of an “N”-shaped $\{\text{W}_6\}$ cluster and a slant $\{\text{Eu}_4\text{W}_2\}$ ring by sharing eight $\mu_2\text{-O}$ atoms is intuitively observed (Fig. 2j and Fig. S9[†]), and the additional two edge lengths of $\text{W}1\cdots\text{Eu}1$ and $\text{W}1\cdots\text{Eu}2$ are 4.162 and 4.268 Å. The $\{\text{W}_6\}$ cluster can be seen as a dimer of the two apex-linked $\{\text{W}_3\text{O}_3\}$ group, where the W2, W8 and W11 group and the W11A, W8A and W2A group respectively form two identical triangles. In the $\{\text{Eu}_4\text{W}_2\}$ ring, four Eu^{3+} ions constitute a regular parallelogram with the edge lengths of 6.265 and 7.290 Å, and two adjacent angles of 88.187° and 91.883°, respectively (Fig. S10[†]). With further capping on the two opposite sides of the parallelogram by W1

and W1A centers, a pseudo-hexagon made up of four Eu and two W centers is ulteriorly constructed as the angle between the parallelogram and triangle (Eu1, Eu2, W1) is as small as 1.342° (Fig. S11†).

Finally, the 3D stacking pattern of **4a** polyanions is also described. It can be observed in Fig. 3 that the **4a** polyanions in the 3D stacking are aligned in an -ABAB- mode (layer A and layer B) along the *b* axis (Fig. 3a and b). Every layer in the *ac* plane features a fascinating wave-shaped arrangement. By visualizing each **4a** polyanion as a rectangle with four vertices as Se1, Se2, Se1A and Se2A atoms, a simplified 3D stacking is presented, from which we can see that layer B can be obtained by rotating **4a** polyanions in layer A by 180° along the *b* axis (Fig. 3c and d). Besides, the 3D stacking along the *c* axis is illustrated in Fig. S12.†

FL properties

Owing to the rich spectroscopic terms of Ln ions, Ln-based materials have gained wide interest in virtue of their unique superiority in FL such as long-lived narrow emission lines, high color purity and quantum efficiencies, as well as significant applications in light-emitting diodes, displays and imaging, optical sensors and devices, *etc.*^{28,39–42} The incorporation of the appropriate fluorescent Ln centers into the POM frameworks can endow POMs with remarkable luminescence

properties. Here, the solid-state FL properties of **3** and **4** at ambient temperature were investigated.

Under excitation at 585 nm, the emission spectrum of **3** was recorded between 800 and 1500 nm in the near-infrared region (Fig. 4a), which shows three peaks at 893, 1057 and 1329 nm, respectively, corresponding to the ${}^4F_{3/2} \rightarrow {}^4I_{9/2}$, ${}^4F_{3/2} \rightarrow {}^4I_{11/2}$ and ${}^4F_{3/2} \rightarrow {}^4I_{13/2}$ transitions of Nd^{3+} ions.⁴³ Notably, the peak at 1057 nm (${}^4F_{3/2} \rightarrow {}^4I_{11/2}$) dominates over the whole spectrum. Meanwhile, by monitoring the emission at 1057 nm, the excitation spectrum of **3** containing several peaks at 526, 585 and 631 nm was recorded (Fig. 4b), and these peaks can be identified as ${}^4I_{9/2} \rightarrow {}^4G_{7/2}$, ${}^4G_{9/2}$, ${}^2K_{13/2}$, ${}^4I_{9/2} \rightarrow {}^2G_{7/2}$, ${}^4G_{5/2}$, and ${}^4I_{9/2} \rightarrow {}^2H_{11/2}$ transitions, respectively.⁴⁴ In addition, the FL lifetime of **3** was measured under the conditions of the strongest excitation ($\lambda_{\text{ex}} = 584$ nm) and emission ($\lambda_{\text{em}} = 1057$ nm), where the lifetime curve obeys a double exponential function with the fitting results of $\tau_1 = 1.65$ μs (34.14%) and $\tau_2 = 10.19$ μs (65.86%), and the average lifetime τ^* was calculated to be 7.22 μs according to the equation $\tau^* = (A_1\tau_1^2 + A_2\tau_2^2)/(A_1\tau_1 + A_2\tau_2)$ (Fig. 4c).⁴⁵ The FL emitting spectrum of **4** was recorded under excitation at 396 nm and exhibits six peaks at 536, 580, 592, 613, 651 and 703 nm, which correspond to the ${}^5D_1 \rightarrow {}^7F_1$, ${}^5D_0 \rightarrow {}^7F_0$, ${}^5D_0 \rightarrow {}^5F_1$, ${}^5D_0 \rightarrow {}^5F_2$, ${}^5D_0 \rightarrow {}^5F_3$ and ${}^5D_0 \rightarrow {}^5F_4$ transitions of Eu^{3+} ions (Fig. 4d).⁴⁶ The excitation spectrum of **4** was obtained through monitoring the

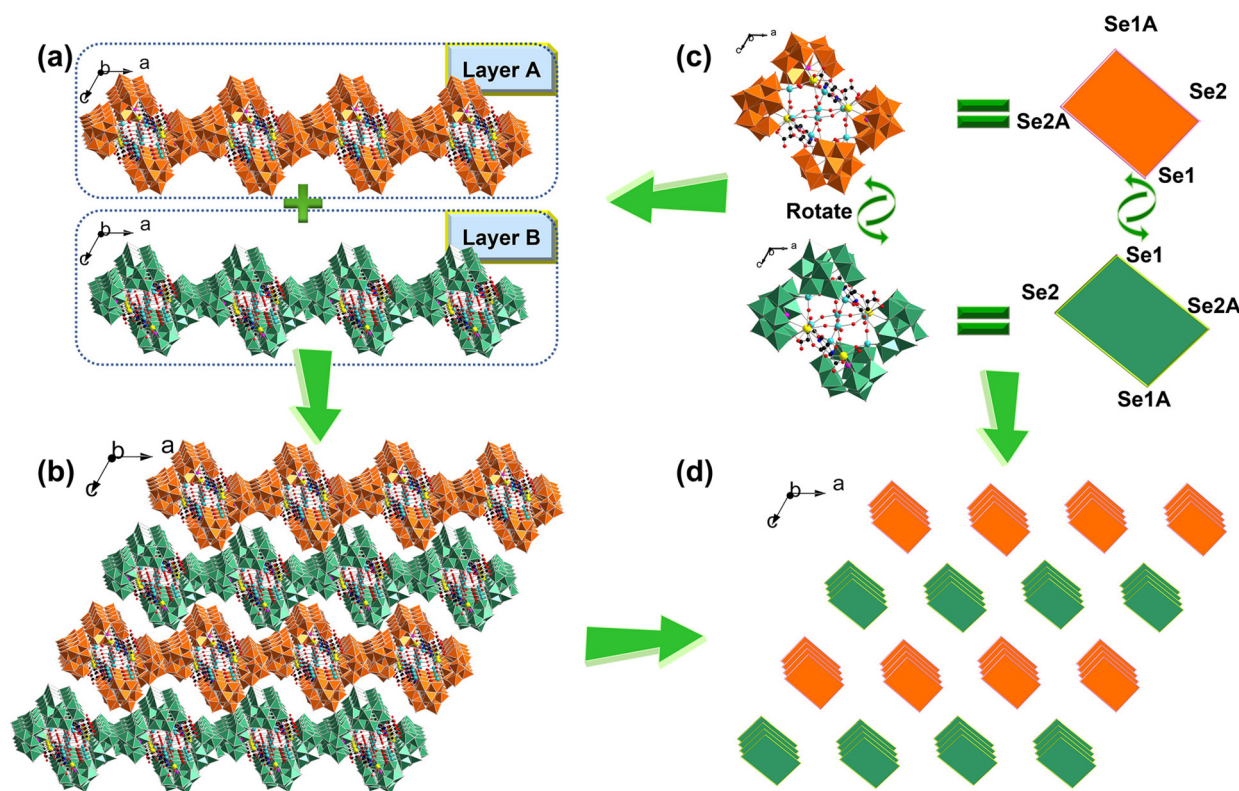


Fig. 3 (a) View of layer A and layer B in the 3D stacking of **4a** polyanions. (b) The 3D stacking view of **4a** along the *b* axis. (c) Simplified models of **4a** polyanions in layer A and layer B. (d) Simplified 3D stacking of **4a** along the *b* axis. Because spatial orientations of **4a** polyanions in layer A and layer B are different, the $\{\text{WO}_6\}$ octahedra in layer A are shown in orange while the $\{\text{WO}_6\}$ octahedra in layer B are shown in sea green.

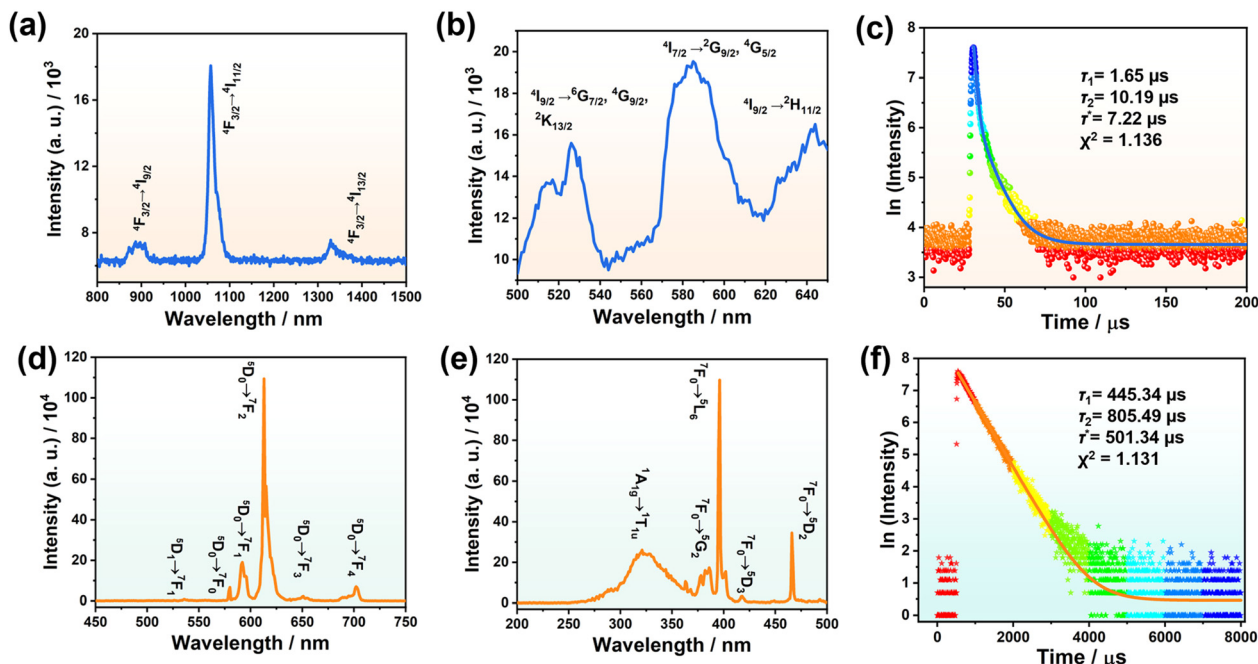


Fig. 4 (a) The NIR emission spectrum of **3** ($\lambda_{\text{ex}} = 584$ nm). (b) The excitation spectrum of **3** ($\lambda_{\text{em}} = 1057$ nm). (c) The lifetime curve of **3** obtained by monitoring the emission at 1057 nm and the excitation at 584 nm. (d) The emission spectrum of **4** ($\lambda_{\text{ex}} = 396$ nm). (e) The excitation spectrum of **4** ($\lambda_{\text{em}} = 613$ nm). (f) The lifetime curve of **4** obtained by monitoring the emission at 613 nm and the excitation at 396 nm.

emission at 613 nm, and the highest intensity peak is located at 396 nm (${}^7F_0 \rightarrow {}^5L_6$) while the other peaks are situated at 320, 386, 417 and 466 nm (${}^1A_{1g} \rightarrow {}^1T_{1u}$, ${}^7F_0 \rightarrow {}^5G_2$, ${}^7F_0 \rightarrow {}^5D_3$ and ${}^7F_0 \rightarrow {}^5D_2$) (Fig. 4e).⁴⁷ Besides, the lifetime curve of **4** obeys a double exponential function with the fitting results of $\tau_1 = 445.34 \mu\text{s}$ (84.45%) and $\tau_2 = 805.49 \mu\text{s}$ (15.55%), and the average τ^* is 501.34 μs (Fig. 4f). As shown in the CIE 1931 chromaticity diagram, **4** exhibits red emission (Fig. S13†).

FL sensing for DPA detection

Bacillus anthracis is a very dangerous bacterium that can cause a serious disease called anthrax through the inhalation of spores, and anthrax spores are also a potential biological warfare agent.^{48,49} Therefore, it is quite indispensable to develop a rapid, accurate, and sensitive detection method. As is known, dipicolinic acid (DPA) is the main marker of anthrax spores and various analytical methods have been applied to detect DPA, such as immunological analysis, electrochemical method, mass spectrometry, biological methods, and so on.^{50–52} However, most of these methods are limited by time/cost consumption and difficult operation of equipment. Recently, a FL sensing technique with rapid and highly efficient detection capability has offered a significant platform for DPA detection.⁵³ Here, we use **4** to construct a FL sensor to detect DPA in aqueous solution and it is necessary to take the structural stability of the **4a** polyanion in aqueous solution into account. Firstly, as revealed by electrospray ionization mass spectrometry (ESI-MS) of **4** in water, three distinct ESI-MS signals appearing at m/z 1183.01 (5⁻), 1479.21 (4⁻) and 1972.32 (3⁻) can be respectively assigned to $\{\text{H}_6(\text{Eu}_2\text{W}_4$

$(\text{H}_2\text{O})_3\text{O}_{11}(\text{HFMA})[\text{SeW}_9\text{O}_{33}]_2\}^{5-}$ (5915.45), $\{\text{H}_7(\text{Eu}_2\text{W}_4(\text{H}_2\text{O})_3\text{O}_{11}(\text{HFMA})[\text{SeW}_9\text{O}_{33}]_2\}^{4-}$ (5916.45) and $\{\text{H}_8(\text{Eu}_2\text{W}_4(\text{H}_2\text{O})_3\text{O}_{11}(\text{HFMA})[\text{SeW}_9\text{O}_{33}]_2\}^{3-}$ (5917.45), suggesting the comparatively good structural stability of the **4a** polyanion with the loss of HPZDA⁻ ligands in water (Fig. S14a†). Moreover, the UV-visible spectral result of **4** in aqueous solution in 48 h can also support the comparatively good structural stability of the **4a** polyanion (Fig. S14b†). Therefore, the benign FL performance together with the water stability drives us to employ **4** as a promising FL probe in water.

The time-varying FL emission spectra of **4** within 48 h in water (3 mg mL⁻¹) were monitored (Fig. 5a). It is evident that the intensity at 613 nm derived from the ${}^5D_0 \rightarrow {}^7F_2$ transition gradually descends in the first 5 h, which is probably caused by dynamic exchange of the water ligands of **4a** polyanions with water molecules in aqueous solution. Then, the emission intensity remains almost unchanged in the following long time from 5 to 48 h, indicating that **4** is suitable to work as a FL probe.

A series of FL titration experiments are helpful to illustrate the sensitivity of **4** (in the following experiments, the concentration of **4** in water is 3 mg mL⁻¹) in the detection of DPA. As demonstrated in Fig. 5b, the consecutive addition of DPA results in the enhancement of the ${}^5D_0 \rightarrow {}^7F_2$ emission intensity of Eu³⁺ ions. In particular, the ${}^5D_0 \rightarrow {}^7F_2$ emission intensity is more sensitive to the introduced DPA, and the intensity (when the concentration of DPA is up to 400 μM) is almost 2-fold higher than that in the absence of DPA. The ratio of $I({}^5D_0 \rightarrow {}^7F_2)/I({}^5D_0 \rightarrow {}^7F_1)$ is a criterion to evaluate the distorted degree of the local symmetry around Eu³⁺ ions. Here, a slight

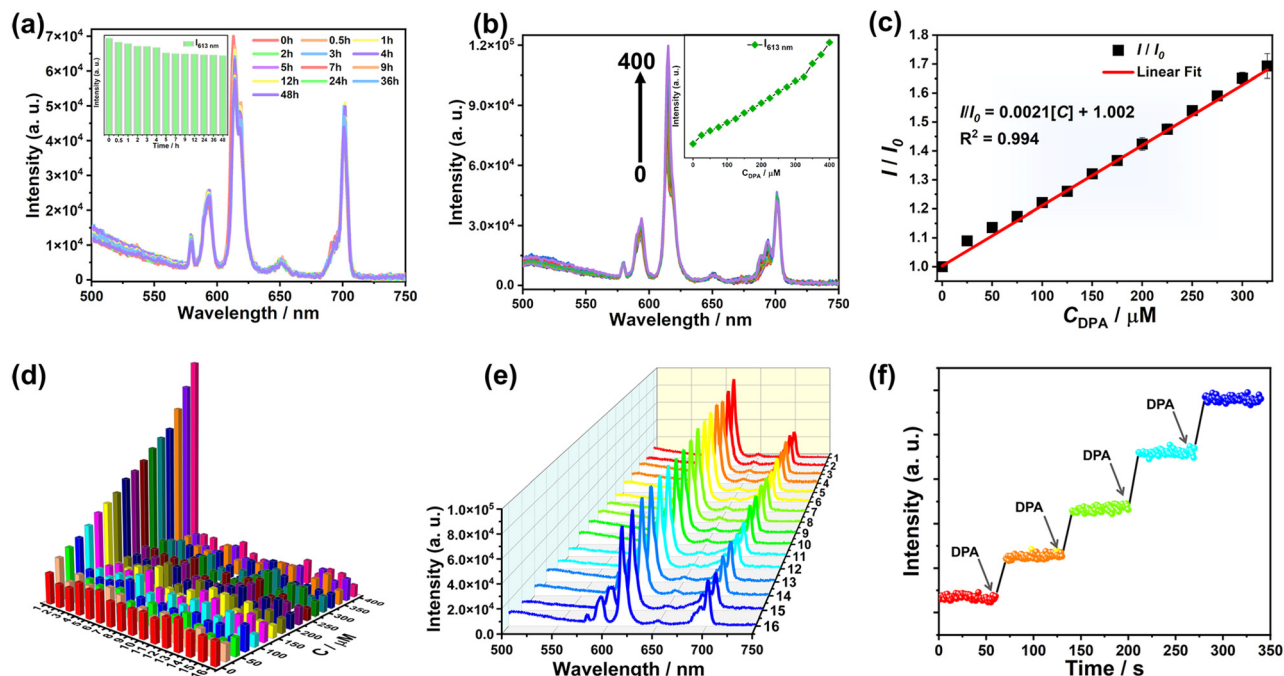


Fig. 5 (a) Time-varying FL emission spectra of **4** (inset: the change of the peak intensity at 613 nm with time). (b) Comparison of the emission spectra of **4** with the addition of different concentrations of DPA (inset: the change of the peak intensity at 613 nm with the DPA concentration). (c) Linear relationship between the I/I_0 ratio and the DPA concentration. (d) Comparison of the FL ${}^5D_0 \rightarrow {}^7F_2$ emission intensity of **4** by the addition of DPA or each interferent with the concentration varying from 0 to 400 μM (in the order: (1) DPA, (2) 2,3-PDCA, (3) 2,5-PDCA, (4) 2-PA, (5) NA, (6) BA, (7) *p*-PA, (8) *m*-PA, (9) H_3BTC , (10) Gly, (11) GSH, (12) K^+ , (13) Mg^{2+} , (14) Ca^{2+} , (15) Cl^- , (16) CH_3COO^-). (e) Comparison of the FL spectra of **4** in the presence of DPA (325 μM) and each different interferent (325 μM) (in the order: (1) DPA, (2) 2,3-PDCA, (3) 2,5-PDCA, (4) 2-PA, (5) NA, (6) BA, (7) *p*-PA, (8) *m*-PA, (9) H_3BTC , (10) Gly, (11) GSH, (12) K^+ , (13) Mg^{2+} , (14) Ca^{2+} , (15) Cl^- , (16) CH_3COO^-). (f) Time scan measurement of the FL response of **4** with the addition of DPA.

alteration in the intensity ratio from 2.6 to 3.8 is observed after titration with DPA (Fig. S15 and Table S2[†]), implying that the local site-symmetry of Eu^{3+} ions slightly changes.⁵⁴ Additionally, a good linear correlation exists between the emission intensity ratio (I/I_0) and the concentration of DPA in the range of 0 to 325 μM , wherein, I_0 and I respectively represent the FL intensity of the ${}^5D_0 \rightarrow {}^7F_2$ transition before and after the addition of DPA. The correlation obeys the equation $I/I_0 = 0.0021C_{\text{DPA}} + 1.002$ ($R^2 = 0.994$) with a limit of detection (LOD) of 3.83 μM (Fig. 5c and Table S3[†]). In addition, on comparing with previous literature reports (Table S4[†]), it is not difficult to find that the LOD (3.83 μM) obtained in this work is relatively higher than some of them, but is obviously below the infectious concentration of anthrax spores (60 μM).⁵⁵ Repeated trials show the good luminescence response and repeatability of **4** to DPA (Fig. S16[†]).

Furthermore, the selectivity and anti-interference ability of **4** for DPA recognition were explored. Some potential interferents including DPA analogues (2,3-pyridine dicarboxylic acid (2,3-PDCA), 2,5-pyridine dicarboxylic acid (2,5-PDCA), 2-picolinic acid (2-PA), nicotinic acid (NA), benzoic acid (BA), *p*-phthalic acid (*p*-PA), *m*-phthalic acid (*m*-PA), 1,3,5-benzenetricarboxylic acid (H_3BTC)), amino acids (glycine (Gly), glutathione (GSH)) (the structural formulae are listed in Scheme S2[†]) and anions/cations were selected. Remarkably, none of them inter-

feres with the recognition and detection of DPA because the ${}^5D_0 \rightarrow {}^7F_2$ emission intensity of **4** is hardly or even negligibly changed by adding each interferent at various dosages (Fig. 5d and S17, S18a, b[†]). Moreover, markedly enhanced luminescence signals can still be acquired when DPA coexists with other interferents (325 μM) (Fig. 5e and S18c[†]). In addition, three interferents (2-PA, Gly and Mg^{2+}) are respectively selected and the lifetime curves of **4** have been tested in the presence of each interferent at different concentrations (Fig. S19[†]). It is obviously observed that the addition of each interferent at different concentrations can hardly change the FL lifetime of **4**. These results clearly indicate that **4** shows outstanding selectivity and anti-interference ability towards the analytical determination of DPA.

In addition, the response time of the FL sensor is also an extremely important parameter for practical use. Therefore, the time scan measurements of the FL response of **4** at the ${}^5D_0 \rightarrow {}^7F_2$ transition were performed at an excitation wavelength of 396 nm. The emission intensity increases instantly and rapidly reaches a steady level within 10 s when DPA is added at a dosage of 100 μM per time (Fig. 5f), which is faster than the majority of reported FL sensors applied to detect DPA (Table S4[†]). This result manifests that **4** can potentially work as a stable and efficient sensor for the quick detection of DPA in biological samples.

To evaluate the practical sensing application, **4** was utilized to detect DPA in tap water and a 10^3 times diluted human serum sample. The detection system was established by adding a sequence of concentrations of DPA in tap water and the human serum sample. It is worth mentioning that the characteristic emission intensity at 613 nm is enhanced by increasing the DPA concentration. The characteristic emission intensity at 613 nm and the DPA concentration in both systems exhibit a good linear relationship with the fitting equation $I = 41\,868.38 + 83.05C_{\text{DPA}}$ ($R^2 = 0.996$) for tap water (Fig. 6a and b) and $I = 55\,210.90 + 146.93C_{\text{DPA}}$ ($R^2 = 0.994$) for the human serum sample (Fig. 6c and d). Based on these equations, the added DPA concentration can be reasonably calculated, and the recoveries (defined as $C_{\text{DPA,cal.}}/C_{\text{DPA,theor.}}$) for detecting DPA in tap water and the human serum sample were determined to be 94.98–99.83% and 96.68–104.35% with the relative standard deviation (RSD, $n = 3$) in the range of 1.20–3.88% and 3.70–6.80%, respectively (Table S5[†]). These results suggest that **4** has great potential as a sensor for detecting DPA in real and complex environments.

Ultimately, to clarify the FL enhancement mechanism of **4** with the addition of DPA, the emission decay dynamics has been studied. In accordance with the FL decay curves, the average lifetime of Eu^{3+} ions (the ${}^5\text{D}_0 \rightarrow {}^7\text{F}_2$ transition) significantly increases from 173.92 to 367.06 μs with the incremental addition of DPA (0–300 μM) (Fig. S20[†]). Considering the strong coordination affinity of DPA towards Eu^{3+} ions owing to its unique coordination sites with three active chelating sites (two carboxyl and one pyridyl groups), we speculate that the FL enhancement mechanism might be attributed to the replacement of coordinate H_2O ligands around Eu^{3+} ions in **4** by DPA, which can effectively inhibit the FL quenching triggered by the O–H oscillators of coordinate H_2O molecules.^{56–58} To verify this hypothesis, the number (q) of coordinate H_2O ligands on the Eu^{3+} ions in **4** was determined by measuring the decay lifetimes in H_2O and D_2O with and without DPA (Fig. 7) according

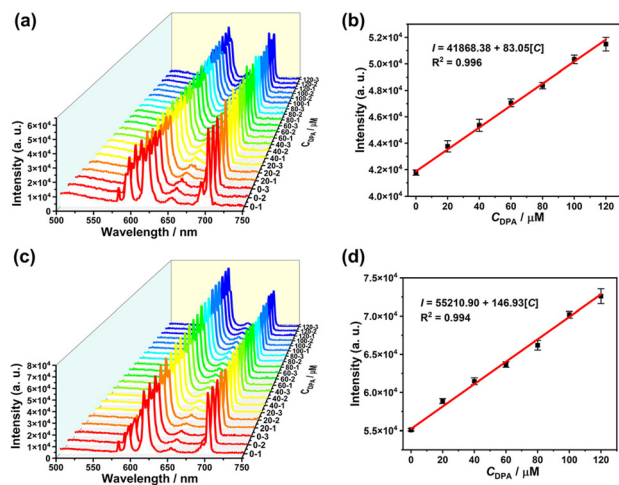


Fig. 6 FL spectra and linear relationships between the emission intensity at 613 nm and the DPA concentration in tap water (a and b) and the human serum sample (c and d).

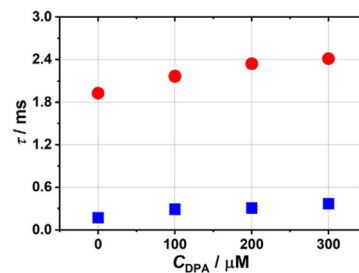


Fig. 7 The lifetimes of **4** in H_2O and D_2O with different DPA concentrations (blue dots represent the H_2O system and red dots represent the D_2O system).

to the equation $q = 1.1 \times [\tau_{\text{H}_2\text{O}}^{-1} - \tau_{\text{D}_2\text{O}}^{-1} - 0.31]$, where $\tau_{\text{H}_2\text{O}}$ and $\tau_{\text{D}_2\text{O}}$ are the lifetimes in H_2O and D_2O environments, respectively, and q was found to be 5.4 in the absence of DPA ($\tau_{\text{H}_2\text{O}} = 0.174$ ms, $\tau_{\text{D}_2\text{O}} = 1.927$ ms), indicating that about five H_2O ligands coordinate with the Eu^{3+} centers (Table 1 and Fig. S21[†]).⁵⁹ With the addition of DPA (100, 200, 300 μM), the decay lifetime progressively increases while q inversely decreases to 2.20 when the DPA concentration is 300 μM ($\tau_{\text{H}_2\text{O}} = 0.367$ ms, $\tau_{\text{D}_2\text{O}} = 2.411$ ms). This result indicates that DPA is more likely to coordinate with the Eu^{3+} ions. Such a coordination environment alteration of the Eu^{3+} ions leads to the enhancement of sensitization and energy transfer. In order to exclude the phenomenon that the Eu^{3+} ions separate from the **4a** polyanions to coordinate with DPA forming simple Eu–DPA complexes in the process of **4** detecting DPA, control experiments in which $\text{Eu}(\text{NO}_3)_3 \cdot 6\text{H}_2\text{O}$ (3 mg mL^{-1}) is used as a FL sensor to detect DPA at different concentrations in H_2O and D_2O have been performed (Fig. S22 and S23a, b[†]). As illustrated in Fig. S22 and S23a, b[†] the ${}^5\text{D}_0 \rightarrow {}^7\text{F}_1$ emission at 592 nm is the strongest and the addition of DPA has a negligible effect on the emission intensity at 592 nm, but, in the process of **4** detecting DPA, the ${}^5\text{D}_0 \rightarrow {}^7\text{F}_2$ emission at 613 nm is the strongest. This comparison can confirm that the Eu^{3+} ions do not separate from the **4a** polyanions to form simple Eu–DPA complexes in the process of **4** detecting DPA. In the meantime, the lifetime curves of $\text{Eu}(\text{NO}_3)_3 \cdot 6\text{H}_2\text{O}$ (3 mg mL^{-1}) in H_2O and D_2O with different DPA concentrations have been measured (Fig. S23c and d[†]). Thus, the number (q) of coordinate H_2O molecules on the Eu^{3+} ions in $\text{Eu}(\text{NO}_3)_3 \cdot 6\text{H}_2\text{O}$ has been calculated to be ca. 9 (Table S6[†]). Moreover, the number of coordinate H_2O molecules on the Eu^{3+} ions does not change with the increase of the DPA concentration. This observation can further confirm that Eu^{3+} ions indeed do not separate

Table 1 Summary of the lifetimes of **4** in H_2O and D_2O with different DPA concentrations and the calculated q values

$C_{\text{DPA}}/\mu\text{M}$	$\tau_{\text{H}_2\text{O}}/\text{ms}$	$\tau_{\text{D}_2\text{O}}/\text{ms}$	q
0	0.174	1.927	5.41
100	0.292	2.165	2.92
200	0.310	2.340	2.74
300	0.367	2.411	2.20

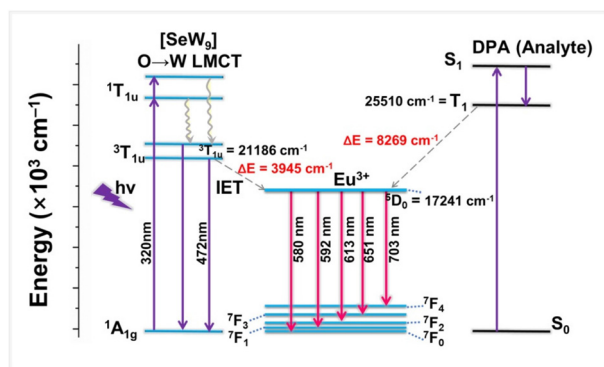


Fig. 8 The energy level diagram exhibiting the proposed energy transfer pathways from the excited triplet states (T_1) of $\{SeW_9\}$ and DPA ligands to the 5D_0 state of the Eu^{3+} ions. IET is internal energy transfer.

from **4a** polyanions to form simple Eu–DPA complexes in the process of **4** detecting DPA. Based on the above analysis, a possible schematic diagram of energy transfer is provided to illustrate the possible mechanism (Fig. 8). Judging by Reinholdt's empirical rule, energy transfer from the analyte to Eu^{3+} ions occurs when the energy gap between the lowest triplet energy level of the analyte and 5D_0 of the Eu^{3+} ion is greater than 3500 cm^{-1} .⁶⁰ In **4**, the emission of Eu^{3+} ions (5D_0 , 17241 cm^{-1}) can be firstly sensitized by $\{SeW_9\}$ building blocks (${}^3T_{1u}$, 21168 cm^{-1}).⁶¹ After the addition of DPA, DPA can chelate with Eu^{3+} ions by substituting coordinate H_2O molecules, and the lowest triplet energy level (T_1 , 25510 cm^{-1}) of DPA can also allow the energy transfer to the Eu^{3+} ions, leading to the emission enhancement of Eu^{3+} ions.⁶²

Conclusions

In summary, a family of unique dual-ligand functionalized dodeca-nuclear Ln–W-cluster incorporated STs **1–4** have been successfully prepared by the cooperative strategy of rigid and flexible ligands. It is noteworthy that **4** can be used as a FL sensor to detect DPA in tap water and a human serum sample, which is also the first time to use the Ln-incorporated ST as a FL probe for the detection of DPA in tap water and a human serum sample. The results demonstrate that **4** can sensitively detect DPA with a low detection limit ($3.83\text{ }\mu\text{M}$), good selectivity and anti-interference and quick response capability in the detection of DPA. This work not only provides a new synthetic strategy for the synthesis of rigid–flexible-ligand functionalized Ln-incorporated POMs, but also presents exploratory research on inorganic–organic hybrid Ln-incorporated POMs applied to fluorescence biological detection of an anthrax biomarker.

Author contributions

Tiantian Gong, Sen Yang and Jiancai Liu performed synthesis, characterization, investigation of photoluminescence pro-

perties and wrote the manuscript. Zixu Wang, Mengyao Li and Siyu Zhang participated in PXRD, IR and TG characterization. Lijuan Chen and Junwei Zhao provided research ideas, determined crystal structures and revised the whole manuscript.

Conflicts of interest

There are no conflicts to declare.

Acknowledgements

This work was supported by the National Natural Science Foundation of China (21871077, 22071042, 22101072, and 22171070), the Program for Innovation Teams in Science and Technology in Universities of Henan Province (20IRTSTHN004), the China Postdoctoral Science Foundation (2021M701067) and the Innovation and Entrepreneurship Training Program for College Students of Henan University (202210475001 and 20222404112).

References

- R. Gao, M. S. Kodaimati and D. P. Yan, Recent advances in persistent luminescence based on molecular hybrid materials, *Chem. Soc. Rev.*, 2021, **50**, 5564.
- S. Parola, B. Julián-López, L. D. Carlos and C. Sanchez, Optical properties of hybrid organic-Inorganic materials and their applications, *Adv. Funct. Mater.*, 2016, **26**, 6506–6544.
- A. V. Artemév, M. P. Davydova, A. S. Berezin, D. G. Samsonenko, I. Y. Bagryanskaya, V. L. Brel, X. Z. Hei, K. A. Brylev, O. I. Artyushin, L. E. Zelenkov, I. I. Shishkin and J. Li, New approach toward dual-emissive organic–inorganic hybrids by integrating Mn(II) and Cu(I) emission centers in ionic crystals, *ACS Appl. Mater. Interfaces*, 2022, **14**, 31000–31009.
- Y. W. Wang, H. X. Li, D. Wang and B. Z. Tang, Inorganic–organic nanocomposites based on aggregation-induced emission luminogens, *Adv. Funct. Mater.*, 2021, **31**, 2006952.
- C. Ritchie, E. G. Moore, M. Speldrich, P. Kögerler and C. Boskovic, Terbium polyoxometalate organic complexes: correlation of structure with luminescence properties, *Angew. Chem., Int. Ed.*, 2010, **49**, 7702–7705.
- J. C. Liu, J. W. Zhao, C. Streb and Y. F. Song, Recent advances on high-nuclear polyoxometalate clusters, *Coord. Chem. Rev.*, 2022, **471**, 214734.
- Y. Zhang, Y. Liu, D. Wang, J. Liu, J. Zhao and L. Chen, State-of-the-art advances in the syntheses, structures, and applications of polyoxometalate-based metal-organic frameworks, *Polyoxometalates*, 2023, **2**, 9140017.
- U. Kortz, A. Müller, J. V. Slageren, J. Schnack, N. S. Dalal and M. Dressel, Polyoxometalates: fascinating structures,

- unique magnetic properties, *Coord. Chem. Rev.*, 2009, **253**, 2315–2327.
- 9 J. Du, Y.-Y. Ma, W.-J. Cui, S.-M. Zhang, Z.-G. Han, R.-H. Li, X.-Q. Han, W. Guan, Y.-H. Wang, Y.-Q. Li, Y. Liu, F.-Y. Yu, K.-Q. Wei, H.-Q. Tan, Z.-H. Kang and Y.-G. Li, Unraveling photocatalytic electron transfer mechanism in polyoxometalate-encapsulated metal-organic frameworks for high-efficient CO₂ reduction reaction, *Appl. Catal., B*, 2022, **318**, 121812.
 - 10 H. P. Xiao, Y. S. Hao, X. X. Li, P. Xu, M. D. Huang and S. T. Zheng, A water-soluble antimony-rich polyoxometalate with broad-spectrum antitumor activities, *Angew. Chem., Int. Ed.*, 2022, e202210019.
 - 11 J. L. Liu, M. Y. Huang, X. Y. Zhang, Z. Y. Hua, Z. R. Feng, Y. Ding, T. D. Sun, X. Sun and C. X. Chen, Polyoxometalate nanomaterials for enhanced reactive oxygen species therapeutics, *Coord. Chem. Rev.*, 2022, **472**, 214785.
 - 12 S. Taleghani, M. Mirzaei, H. Eshtiagh-Hosseini and A. Frontera, Tuning the topology of hybrid inorganic-organic materials based on the study of flexible ligands and negative charge of polyoxometalates: a crystal engineering perspective, *Coord. Chem. Rev.*, 2016, **309**, 84–106.
 - 13 L. Fu, H. Q. Gao, M. Yan, S. Z. Li, X. Y. Li, Z. F. Dai and S. Q. Liu, Polyoxometalate-based organic-inorganic hybrids as antitumor drugs, *Small*, 2015, **11**, 2938–2945.
 - 14 J.-C. Liu, J.-F. Wang, Q. Han, P. Shangguan, L.-L. Liu, L.-J. Chen, J.-W. Zhao, C. Streb and Y.-F. Song, Multicomponent self-assembly of a giant heterometallic polyoxotungstate supercluster with antitumor activity, *Angew. Chem., Int. Ed.*, 2021, **60**, 11153–11157.
 - 15 C. L. Lv, R. N. N. Khan, J. Zhang, J. J. Hu, J. Hao and Y. G. Wei, Bifunctionalization of polyoxometalates with two different organoimido ligands, *Chem. – Eur. J.*, 2013, **19**, 1174–1178.
 - 16 W. M. Xuan, R. Pow, N. Watfa, Q. Zheng, A. J. Surman, D.-L. Long and L. Cronin, Stereoselective assembly of gigantic chiral molybdenum blue wheels using lanthanide ions and amino acids, *J. Am. Chem. Soc.*, 2019, **141**, 1242–1250.
 - 17 B. Li and L. X. Wu, Perspective of polyoxometalate complexes on flexible assembly and integrated potentials, *Polyoxometalates*, 2023, **2**, 9140016.
 - 18 L. L. Liu, J. Jiang, G. P. Liu, X. D. Jia, L. J. Chen, J. W. Zhao and P. Yang, Hexameric to trimeric lanthanide-included selenotungstates and their 2D honeycomb organic-inorganic hybrid films used for detecting ochratoxin A, *ACS Appl. Mater. Interfaces*, 2021, **13**, 35997–36010.
 - 19 Q. Han, Z. Li, X. M. Liang, Y. Ding and S.-T. Zheng, Synthesis of a 6-nm-long transition-metal-rare-earth-containing polyoxometalate, *Inorg. Chem.*, 2019, **58**, 12534–12537.
 - 20 X. D. Jia, J. Jiang, L. L. Liu, L. N. Meng, L. J. Chen and J. W. Zhao, Two innovative fumaric acid bridging lanthanide-encapsulated hexameric selenotungstates containing mixed building units and electrochemical performance for detecting mycotoxin, *Inorg. Chem.*, 2022, **61**, 10965–10976.
 - 21 F. Hussain, R. W. Gable, M. Speldrich, P. Kgerler and C. Boskovic, Polyoxotungstate-encapsulated Gd₆ and Yb₁₀ complexes, *Chem. Commun.*, 2009, 328–330.
 - 22 L. L. Liu, J. Jiang, L. M. Cui, J. W. Zhao, X. H. Cao and L. J. Chen, Double trigonal pyramidal {SeO₃} groups bridged 2-picolinic acid modified cerium-inlaid polyoxometalate including mixed selenotungstate subunits for electrochemically sensing ochratoxin A, *Inorg. Chem.*, 2022, **61**, 1949–1960.
 - 23 S. T. Zheng, J. Zhang, X. X. Li, W. H. Fang and G. Y. Yang, Cubic polyoxometalate-organic molecular cage, *J. Am. Chem. Soc.*, 2010, **132**, 15102–15103.
 - 24 Y.-H. Xiao, Z.-P. Deng, Z.-B. Zhu, L.-H. Huo and S. Gao, Rare earth metal-organic complexes constructed from hydroxyl and carboxyl modified arenesulfonate: syntheses, structure evolutions, and ultraviolet, visible and near-infrared luminescence, *Dalton Trans.*, 2017, **46**, 16493–16504.
 - 25 C. M. Granadeiro, D. Julião, S. O. Ribeiro, L. Cunha-Silva and S. S. Balula, Recent advances in lanthanide-coordinated polyoxometalates: from structural overview to functional materials, *Coord. Chem. Rev.*, 2023, **476**, 214914.
 - 26 A. A. Ansari, A. K. Parchur, M. K. Nazeeruddin and M. M. Tavakoli, Luminescent lanthanide nanocomposites in thermometry: Chemistry of dopant ions and host matrices, *Coord. Chem. Rev.*, 2021, **444**, 214040.
 - 27 Y. Huo, Y.-C. Chen, J.-L. Liu, J.-H. Jia, W.-B. Chen, S.-G. Wu and M.-L. Tong, A wheel-shaped Dy(III) single-molecule magnet supported by polyoxotungstates, *Dalton Trans.*, 2017, **46**, 16796–16801.
 - 28 J. H. Liu, L. D. Lin, G. Q. Wang, L. Y. Li, Y. Q. Sun, X. X. Li and S. T. Zheng, All-inorganic open frameworks based on gigantic four-shell Ln@W₈@Ln₈@(SiW₁₂)₆ clusters, *Chem. Commun.*, 2020, **56**, 10305–10308.
 - 29 D. Wang, J. Jiang, M.-Y. Cao, S.-S. Xie, Y.-M. Li, L.-J. Chen, J.-W. Zhao and G.-Y. Yang, An unprecedented dumbbell-shaped pentadeca-nuclear W–Er heterometal cluster stabilizing nanoscale hexameric arsenotungstate aggregate and electrochemical sensing properties of its conductive hybrid film-modified electrode, *Nano Res.*, 2022, **15**, 3628–3637.
 - 30 S. W. Zhang, J. W. Zhao, P. T. Ma, J. Y. Niu and J. P. Wang, Rare-earth-transition-metal organic-inorganic hybrids based on Keggin-type polyoxometalates and pyrazine-2,3-dicarboxylate, *Chem. – Asian J.*, 2012, **7**, 966–974.
 - 31 Q. Han, J. C. Liu, Y. Wen, L. J. Chen, J. W. Zhao and G. Y. Yang, Tellurotungstate-based organotin-rare-earth heterometallic hybrids with four organic components, *Inorg. Chem.*, 2017, **56**, 7257–7269.
 - 32 J. C. Liu, J. W. Zhao and Y. F. Song, 1-D chain tungstotellurate hybrids constructed from organic ligand-connecting iron-lanthanide heterometal encapsulated tetrameric polyoxotungstate units, *Inorg. Chem.*, 2019, **58**, 9706–9712.
 - 33 J. Gao, J. Yan, S. Beeg, D.-L. Long and L. Cronin, One-pot versus sequential reactions in the self-assembly of gigantic nanoscale polyoxotungstates, *J. Am. Chem. Soc.*, 2013, **135**, 1796–1805.

- 34 J. Yan, D.-L. Long and L. Cronin, Development of a building block strategy to access gigantic nanoscale heteropolyoxotungstates by using SeO_3^{2-} as a template linker, *Angew. Chem., Int. Ed.*, 2010, **49**, 4117–4120.
- 35 W.-C. Chen, C.-Q. Jiao, X.-L. Wang, K.-Z. Shao and Z.-M. Su, Self-assembly of nanoscale lanthanoid-containing selenotungstates: synthesis, structures, and magnetic studies, *Inorg. Chem.*, 2019, **58**, 12895–12904.
- 36 Y. J. Liu, H. L. Li, C. T. Li, P. J. Gong, X. Y. Ma, L. J. Chen and J. W. Zhao, Organocounterions-assisted and pH-controlled self-assembly of five nanoscale high-nuclear lanthanide substituted heteropolytungstates, *Cryst. Growth Des.*, 2017, **17**, 3917–3928.
- 37 J. Jiang, L. L. Liu, G. P. Liu, D. Wang, Y. Zhang, L. J. Chen and J. W. Zhao, Organic–inorganic hybrid cerium-encapsulated selenotungstate including three building blocks and its electrochemical detection of dopamine and paracetamol, *Inorg. Chem.*, 2020, **59**, 15355–15364.
- 38 G. P. Liu, L. L. Liu, T. T. Gong, Y. Z. Li, L. J. Chen and J. W. Zhao, Nicotinic-acid-ornamented tetrameric rare-earth-substituted phospho(III)tungstates with the coexistence of mixed Keggin/Dawson building blocks and its honeycomb nanofilm for detecting toxins, *Inorg. Chem.*, 2021, **60**, 14457–14466.
- 39 Y. K. Huang, X. Y. Zhai, T. F. Ma, M. Z. Zhang, H. B. Pan, W. W. Lu, X. L. Zhao, T. W. Sun, Y. Q. Li, J. Shen, C. H. Yan and Y. P. Du, Rare earth-based materials for bone regeneration: breakthroughs and advantages, *Coord. Chem. Rev.*, 2022, **450**, 214236.
- 40 A. K. Singh, Multifunctionality of lanthanide-based luminescent hybrid materials, *Coord. Chem. Rev.*, 2022, **455**, 214365.
- 41 L. B. Yang, J. J. Luo, L. Gao, B. X. Song and J. Tang, Inorganic lanthanide compounds with f-d transition: from materials to electroluminescence devices, *J. Phys. Chem. Lett.*, 2022, **13**, 4365–4373.
- 42 Q. Wang, G. X. Chen, Z. H. Yu, X. P. Ouyang and J. F. Tian, Photoluminescent composites of lanthanide-based nanocrystal-functionalized cellulose fibers for anticounterfeiting, *ACS Sustainable Chem. Eng.*, 2018, **6**, 13960–13967.
- 43 W. X. Hao, X. P. Yang, Y. N. Ma, M. Y. Niu, D. L. Shi and D. Schipper, Construction of a high-nuclearity Nd(III) nanoring for the NIR luminescent detection of antibiotics, *Dalton Trans.*, 2021, **50**, 5865.
- 44 H.-L. Li, Y.-J. Liu, J.-L. Liu, L.-J. Chen, J.-W. Zhao and G.-Y. Yang, Structural transformation from dimerization to tetramerization of serine-decorated rare-earth-incorporated arsenotungstates induced by the usage of rare-earth salts, *Chem. – Eur. J.*, 2017, **23**, 2673–2689.
- 45 X. Xu, X. Y. Liu, D. Wang, X. J. Liu, L. J. Chen and J. W. Zhao, $\{\text{HPO}_3\}$ and $\{\text{WO}_4\}$ simultaneously inducing assembly of tri-Ln(III)-incorporated antimonotungstates and their photoluminescence behaviors, *Inorg. Chem.*, 2021, **60**, 1037–1044.
- 46 Z. J. Fu, W. M. Gao, T. Yu and L. H. Bi, Study of bi-directional detection for ascorbic acid and sodium nitrite based on Eu-containing luminescent polyoxometalate, *Talanta*, 2019, **195**, 463–471.
- 47 S.-M. Liu, Z. Zhang, X.-H. Li, H.-J. Jia and S.-X. Liu, Synthesis and photophysical properties of crystalline $[\text{EuW}_{10}\text{O}_{36}]^{9-}$ -based polyoxometalates with lanthanide ions as counter cations, *J. Alloys Compd.*, 2018, **761**, 52–57.
- 48 K. L. Ai, B. H. Zhang and L. H. Lu, Europium-based fluorescence nanoparticle sensor for rapid and ultrasensitive detection of an anthrax biomarker, *Angew. Chem., Int. Ed.*, 2009, **48**, 304–308.
- 49 Y. H. Zhang, B. Li, H. P. Ma, L. M. Zhang, H. Jiang, H. Song, L. G. Zhang and Y. S. Lou, A nanoscaled lanthanide metal–organic framework as a colorimetric fluorescence sensor for dipicolinic acid based on modulating energy transfer, *J. Mater. Chem. C*, 2016, **4**, 7294–7301.
- 50 I. N. Larkin, V. Garmella, G. Yamankurt, A. W. Scott, H. Xing and C. A. Mirkin, Dual-readout sandwich immunoassay for device-free and highly sensitive anthrax biomarker detection, *Anal. Chem.*, 2020, **92**, 7845–7851.
- 51 M. K. Sharma, J. Narayanan, D. Pardasani, D. N. Srivastava, S. Upadhyay and A. K. Goel, Ultrasensitive electrochemical immunoassay for surface array protein, a bacillus anthracis biomarker using Au–Pd nanocrystals loaded on boron-nitride nanosheets as catalytic labels, *Biosens. Bioelectron.*, 2016, **80**, 442–449.
- 52 R. V. Misra, N. Z. Ahmod, R. Parker, M. Fang, H. Shah and S. Gharbia, Developing an integrated proteo-genomic approach for the characterisation of biomarkers for the identification of bacillus anthracis, *J. Microbiol. Methods*, 2022, **88**, 237–247.
- 53 M. Donmez, H. A. Oktem and M. D. Yilmaz, Ratiometric fluorescence detection of an anthrax biomarker with Eu^{3+} -chelated chitosan biopolymers, *Carbohydr. Polym.*, 2018, **180**, 226–230.
- 54 Z. Abbas and A. K. Patra, Luminescent β -diketonate coordinated europium(III) sensor for rapid and sensitive detection of Bacillus Anthracis biomarker, *J. Lumin.*, 2022, **244**, 119726.
- 55 X. Q. Li, J. J. Luo, L. Feng, F. H. Ma and M. H. Yang, In-situ incorporation of fluorophores in zeolitic imidazolate framework-8 (ZIF-8) for ratio-dependent detecting a biomarker of anthrax spores, *Anal. Chem.*, 2020, **92**, 7114–7122.
- 56 M. Na, S. P. Zhang, J. J. Liu, S. D. Ma, Y. X. Han, Y. Wang, Y. X. He, H. L. Chen and X. G. Chen, Determination of pathogenic bacteria—bacillus anthrax spores in environmental samples by ratiometric fluorescence and test paper based on dual-emission fluorescent silicon nanoparticles, *J. Hazard. Mater.*, 2020, **386**, 121956.
- 57 X. Wang, Y. Wang, X. Y. Wang, C. Y. Hu, X. J. Wu, W. Guo, S. J. Zhen, C. Z. Huang and Y. F. Li, Dual-ligand two-dimensional europium-organic gels nanosheets for ratiometric fluorescence detecting anthrax spore biomarker, *Chem. Eng. J.*, 2022, **435**, 134912.
- 58 R. Zhou, Q. Zhao, K.-K. Liu, Y.-J. Lu, L. Dong and C.-X. Shan, Europium-decorated ZnO quantum dots as a

- fluorescent sensor for the detection of an anthrax biomarker, *J. Mater. Chem. C*, 2017, **5**, 1685–1691.
- 59 K.-Y. Wang, B. S. Bassil, Z. G. Lin, I. Römer, S. Vanhaecht, T. N. Parac-Vogt, C. S. D. Pipaón, J. R. Galán-Mascaórs, L. Y. Fan, J. Cao and U. Kortz, Ln₁₂-containing 60-tungstogermanates: synthesis, structure, luminescence, and magnetic studies, *Chem. – Eur. J.*, 2015, **21**, 18168–18176.
- 60 P. P. Huo, Z. J. Li, R. H. Yao, Y. H. Deng, C. C. Gong, D. B. Zhang, C. B. Fan and S. Z. Pu, Dual-ligand lanthanide metal–organic framework for ratiometric fluorescence detection of the anthrax biomarker dipicolinic acid, *Spectrochim. Acta, Part A*, 2022, **282**, 121700.
- 61 T. T. Gong, J. Jiang, S. Yang, J. C. Liu, L. J. Chen and J. W. Zhao, Lanthanide-incorporated polyoxometalates assembled from mixed-heteroatom-oriented three-layered cage clusters, *Inorg. Chem.*, 2022, **61**, 18147–18153.
- 62 J. Othong, J. Boonmak, F. Kielar, S. Hadsadee, S. Jungstittiwong and S. Youngme, Self-calibrating sensor with logic gate operation for anthrax biomarker based on nanoscaled bimetallic lanthanoid MOF, *Sens. Actuators, B*, 2020, **316**, 128156.